

Quantitative Evaluations on Saliency Methods: An Experimental Study

Xiao-Hui Li
Huawei Technologies
Shenzhen, China
lixiaohui33@huawei.com

Yuhan Shi
Huawei Technologies
Shenzhen, China
shiyuhan1@huawei.com

Haoyang Li
Huawei Technologies
Hong Kong SAR, China
li.haoyang@huawei.com

Wei Bai
Huawei Technologies
Hong Kong SAR, China
baiwei16@huawei.com

Yuanwei Song
Huawei Technologies
Hong Kong SAR, China
song.yuanwei@huawei.com

Caleb Chen Cao
Huawei Technologies
Hong Kong SAR, China
caleb.cao@huawei.com

Lei Chen
Hong Kong University of Science and
Technology
Hong Kong SAR, China
leichen@cse.ust.hk

Abstract

It has been long debated that eXplainable AI (XAI) is an important topic, but it lacks rigorous definition and fair metrics. In this paper, we briefly summarize the status quo of the metrics, along with an exhaustive experimental study based on them, including faithfulness, localization, false-positives, sensitivity check, and stability. With the experimental results, we conclude that among all the methods we compare, no single explanation method dominates others in all metrics. Nonetheless, Gradient-weighted Class Activation Mapping (Grad-CAM) and Randomly Input Sampling for Explanation (RISE) perform fairly well in most of the metrics. Utilizing a set of filtered metrics, we further present a case study to diagnose the classification bases for models. While providing a comprehensive experimental study of metrics, we also examine measuring factors that are missed in current metrics and hope this valuable work could serve as a guide for future research.

CCS Concepts: • General and reference → Metrics; • Human-centered computing → Heat maps; Visualization design and evaluation methods; • Computing methodologies → Artificial intelligence.

Keywords: eXplainable Artificial Intelligence, Metrics, Evaluation, Model Diagnosis

1 Introduction

Artificial Intelligence (AI) technology has gained tremendous development in the past decade, especially in computer vision (CV) community [36]. Since the birth of AlexNet [12], deep learning (DL) based methods have outperformed traditional methods and can even beat human beings in many

open challenges (e.g. ImageNet image-classification challenge [27], COCO object-detection challenge [15]). However, the high non-linearity and complexity make these models black-boxes, i.e., it is difficult for humans to understand their internal working mechanisms and decision-making processes. Such intransparency has raised concerns not only among the related industries but also among governments and organizations.

As a result, XAI has emerged as an important and popular research direction among academia in the past few years [1, 14, 37]. An exponentially increasing number of scientific works have been conducted to push forward this branch of research [3, 16, 20, 29, 30]. In CV scenario, a very natural way to provide explanations is through visualization. Among visualization, one of the most popular branches is through generating *saliency map* that shows the importance of input features towards the final output on the pixel/super-pixel level, e.g. Grad-CAM [30] and SHapley Additive exPlanations (SHAP) [16], Local Interpretable Model-agnostic Explanations (LIME) [26]. Compared to other visualization methods such as feature visualization [19], saliency methods are usually simpler and easier to deploy. Besides, the explanation of saliency map is within the input space where the value of the saliency map at a specific position directly indicates the importance of that pixel and is thus usually more intuitive.

As tools explaining the decision-making process, XAI methods can be applied in human-in-the-loop machine learning systems [11, 21, 23] or model debugging systems [17, 29, 35]. However, to deploy XAI methods in practical systems, a methodological challenge appears: *how to evaluate these methods such that the users can choose the most suitable one for their needs.*

From the perspective of experiments conduction for accessing XAI methods, the corresponding evaluation metrics can be grouped into human-grounded metrics and functionally-grounded ones [5]. Human-grounded metrics are usually designed through human-involving experiments, e.g. designing questionnaires for the explanations and invite a group of tester to answer them. Collecting their answers and a quantified evaluation result can be obtained [9]. However, it is difficult to scale up such experiments for big data scenario as human participants can be costive and hard to standardize. In this sense, functionally-grounded metrics that do not involve human testers might be a better choice for large scale data. Along this path, different metrics have been proposed to quantify different properties of XAI methods.

A few works quantified the *faithfulness* of explanations. [22, 28] proposed area over/under perturbation curve as metrics of faithfulness when removing/inserting important features the explainer indicates. Some alternative works quantified the *localization* ability of saliency methods. Simonyan *et al.* [41] proposed Pointing Game (PG) which counts the ratio of data samples in which the pixel with the highest relevance score lies in the bounding box. Starting from constructing controllable "ground-truth" for explanations, Yang and Kim [38] proposed three metrics to evaluate *false-positives* of explanations based this dataset: Model Contrast Score (MCS), Input dependence Rate (IDR) and Input Independence Rate (IIR). Some other works studied if XAI methods have certain desired sensitivities (we term it *sensitivity check*). [2] proposed to check whether the XAI methods are sensitive to model weights and [24] proposed to check the class sensitivity of the XAI methods. In contrast to desired sensitivities, there are works propose to check the *stability* of XAI methods towards undesired variations (e.g., insignificant noise on the input), [4, 18, 39] proposed different but similar metrics by perturbing the input slightly and measure the corresponding difference on the explanation.

Although these metrics have been developed, an overall quantitative comparison with all these metrics among the widely used XAI methods, e.g. Grad-CAM, has not yet been conducted. In this work, we aim to fill in this gap by performing extensive experiments to compare these different saliency methods with the proposed metrics. As we start from large scale datasets, in this paper, we only consider computational metrics as mentioned above. Hopefully, our results can serve as a guide to choose a suitable method for a given use-case. Our main contributions are as follows:

- A thorough quantitative evaluation based on different metrics is conducted to compare some of the widely deployed XAI methods that generate saliency maps as explanations. With the experimental results, we conclude the pros and cons of these methods.
- We provide strategic augmentation of the benchmark dataset [38] to adapt to more objects and more scenes.

- We modify the PG metric for localization and the MCS metric for false-positives to enhance their testing usability.
- We present a case study of the XAI methods and metrics in actual model analysis, which helps diagnose the spurious correlations in the dataset.

Outline. This rest of this paper is organized as the following: we first review some of the popular and widely discussed XAI methods that generate saliency maps. After that, we introduce the definition and calculation of the proposed evaluation metrics, summarizing the advantages and disadvantages of them as evaluation metrics. Based on these metrics, we conduct an exhaustive comparative experiment on the methods reviewed in Section. 2 with different benchmark datasets and black-box models. The experimental results and findings are reported in Section. 4. Following the experimental results, we present a simple utilization of the metrics and XAI methods in Section 5. Finally, we conclude and highlight the future work in Section. 6.

2 Saliency Methods

Saliency methods are popular explainers, especially in image classification scenario. These explainers quantify the "importance" of individual pixels w.r.t the final out and generate a visualized saliency map in pixel/input space. From the mechanism of computing such "importance", these methods can be grouped into two categories: 1. Backpropagation methods: the relevance is calculated through backpropagation; 2. Perturbation-based methods: the importance of a certain pixel is quantified as the output drop when perturbing this pixel. With the efforts of scientists in this community, plenty of innovative methods have been proposed to generate high-quality saliency maps. In this section, we review some of the most widely used methods according to the aforementioned categories.

In the following descriptions, an input image is represented as $I \in \mathbb{R}^{ch \times h \times w}$, where ch, h, w are the number of channels, height, and width of the input image. A black-box classifier can be described as a function $f : \mathbb{R}^{ch \times h \times w} \rightarrow \mathbb{R}^C$, where C is the number of classes in the image classification problem. An explanation method that generates the saliency map for the input image and black-box model is represented as a functional $E : (\mathbb{R}^{ch \times h \times w}, f) \rightarrow \mathbb{R}^{h \times w}$, where the output saliency map has the same spatial dimension as the input image.

2.1 Backpropagation Methods

The basic idea of backpropagation methods is to compute class-relevance of individual pixels by propagating the quantity of interest (e.g. gradients, relevance, excitation) back to the input image space. The claim is that the higher the value of the propagated signal at a particular pixel, the more important that pixel is to the final output.

2.1.1 Gradient. Proposed by Simonyan *et al.*, Gradient directly computes the gradients of the output class w.r.t the input pixels of a given image as the explanation [31]. Specifically, following the definition in [31], the saliency map for class c can be calculated as follows :

$$E_{Gradient}(I, f)_c = \left. \frac{\partial f_c(I')}{\partial I'} \right|_{I'=I}. \quad (1)$$

This formulation can also be understood as: $f_c(I')$ can be approximated with a linear function in the neighborhood of I by the first-order Taylor expansion: $f_c(I') \approx E(I, f)_c^T \cdot (I' - I) + b$. The weights of this approximated linear function are the generated saliency map.

2.1.2 Guided Backpropagation. Despite the simplicity of Gradient method, the generated saliency maps are usually noisy and difficult to understand. To overcome this issue, Springenberg *et al.* proposed Guided Backpropagation (GBP) with an additional guidance signal from the higher layers [33]. It prevents backward flow of negative gradients, which decreases the activation of the higher layer unit. Denoting $\{A_0, A_1, \dots, A_k\}$ as the feature maps during the forward pass at each layer, and $\{R_0, R_1, \dots, R_k\}$ as the signal obtained in the backward pass, GBP zeros out negative gradients during the backpropagation of R as follows:

$$GBP : R^i = (A^i > 0) \cdot (R^{i+1} > 0) \cdot R^{i+1} \quad (2)$$

where $(A^i > 0)$ keeps only the positive activations, and $(R^{i+1} > 0)$ keeps the positive gradients only. Starting from the last layer and iterating Equation. (2) until $i = 0$, the saliency map can then be obtained as $E_{GBP}(I, f) = R^0$.

2.1.3 Integrated Gradients. Gradient method suffers from another issue called "gradient saturation" that gradient vanishes with certain value of input and cannot represent the sensitivity of this input. Integrated gradients (IntGrad) [34] addresses this issue by summing over scaled versions of inputs. Introducing a baseline input I' , IntGrads are defined as the path integral of the gradient along the straight line path from the baseline I' to the input I :

$$E_{IntGrad}(I, f) = (I - I') \times \int_{\alpha=0}^1 \frac{\partial f(I' + \alpha \times (I - I'))}{\partial I} d\alpha \quad (3)$$

For images, the baseline could be an image with constant value or an image respecting an empirical distribution.

2.1.4 Grad-CAM. Introduced by Selvaraju *et al.*, Grad-CAM uses the class-specific gradient flowing into the last convolutional layer of a CNN model (rather than flowing back to input as in Gradient method) to produce a coarse localization map of the important regions in the image [30]. It is a generalization of Class Activation Mapping (CAM) [42] where CAM requires global average pooling layer on the fully CNN models while Grad-CAM can be applied to CNN models with fully connected layers. As shown in Figure. 1, in order to get the class-discriminative localization map,

the first step is to compute the gradient of the score for class c , y^c (before softmax) with respect to feature maps A^k of a convolutional layer. Then the neuron importance weights are calculated:

$$a_k^c = \frac{1}{Z} \sum_i \sum_j \frac{\partial y^c}{\partial A_{ij}^k} \quad (4)$$

The weight a_k^c represents the importance of feature map A^k for a specific class c . Then, performing a weighted combination of forward activation maps followed by a ReLU operation, saliency maps are generated through:

$$E_{Grad-CAM}(I, f)_c = \text{ReLU}\left(\sum_k a_k^c A^k\right) \quad (5)$$

The application of ReLU here is to focus on features with positive influence on the class of interest. In most of the use-cases, the feature maps A^k are set to be the activation maps of the last convolutional layer.

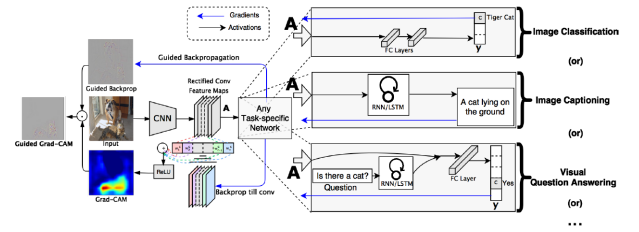


Figure 1. Grad-CAM Overview : Given an image and a target class, the image is fed into the network and the activation maps for the layers of interest are obtained. A one-hot signal with desired class set to 1 is then backpropagated to the rectified convolutional feature maps of interest, which is combined to compute the coarse Grad-CAM saliency map. [30]

2.1.5 Contrastive Excitation Backpropagation. Like Grad-CAM, Excitation Backpropagation [41] also generates interpretable attention maps at intermediate convolutional layers. Different from the former methods that back propagate the gradients, Excitation Backpropagation defines a top-down propagation rule through excitatory connections between activation neurons as follows:

$$P(a_j|a_i) = \begin{cases} Z_i \hat{a}_j w_{ji} & \text{if } w_{ji} \geq 0 \\ 0 & \text{Otherwise} \end{cases} \quad (6)$$

where \hat{a}_j is the activation function coming from lower layer, w_{ij} is the weight from neuron i to neuron j . $Z_i = 1/\sum_{j:w_{ji} \geq 0} \hat{a}_j w_{ji}$ is a normalization factor. Saliency map can be computed from any intermediate convolutional layers by recursively propagating the top-down signal layer by layer through Equation. (6), then taking the sum across channels. Contrastive Excitation Backpropagation (CEBP) inherits the idea of Excitation

Backpropagation and adopts the idea of contrasting the excitation of one class with ones of all the others. This further enhances the class discriminative maps. To do this, given an output unit $o_i \in O$, a dual unit $\bar{o}_i \in O$ is virtually constructed, whose input weights are the negation of those of o_i . For example, if an output unit corresponds to an "elephant" classifier, then its dual unit will correspond to a non-"elephant" classifier. By subtracting the saliency map for \bar{o}_i from the one for o_i will cancel out common winner neurons and enhanced the discriminative neurons. Finally, the result is contrastive saliency map, which better highlights the regions making the image unique to the target class.

2.2 Perturbation-based Methods

The aforementioned backpropagation methods require access to the internals of the model to be explained, such as the gradients of the output w.r.t the input, intermediate feature maps, or the network's weights. On the contrary, perturbation-based methods are truly "black-box" methods. The saliency map is generated by perturbing the input and observing its effects on the output. Without actual access to the structures or internal states of the models, perturbation-based methods are therefore model-agnostic.

2.2.1 Occlusion. Occlusion [40] is a visualization technique that answering if the black-box model is truly identifying the location of the object in the image or just using the surrounding context. Specifically, it systematically replaces different contiguous rectangular regions of the input image with a baseline input value, and monitors how the feature maps and classifier outputs changes. The saliency map for a specific class c can be calculated by Equation. (7):

$$E_{Occlusion}(I, f)_c = \sum_k \frac{f_c(I) - f_c(I'_k)}{m \times m} \mathbb{I}_k \quad (7)$$

where I'_k is an perturbed image masked by an $m \times m$ square and \mathbb{I}_k is an indicator function that for pixels within the square region $\mathbb{I}_k = 1$, otherwise $\mathbb{I}_k = 0$. For features located in multiple regions, the corresponding output differences are averaged to compute the attribution for that feature.

2.2.2 RISE. Randomized Input Sampling for Explanation (RISE) generates saliency maps by sampling on multiple random binary masks. As shown in Figure. 2, the original image is randomly masked, and then fed into the black-box model and gets a prediction. The final saliency map is the weighted sum of these random masks, with the weights being the corresponding output on the node of interest:

$$E_{RISE}(I, f)_c = \sum_i f_c(I \odot M_i) M_i \quad (8)$$

where c is the class of interest, M_i is the random mask and \odot is element-wise product in spatial dimensions. The idea behind this is that if a mask preserves important parts of the image, it gets a higher score on the output, and consequently

has a higher weight and a more dominant contribution on the final saliency map.

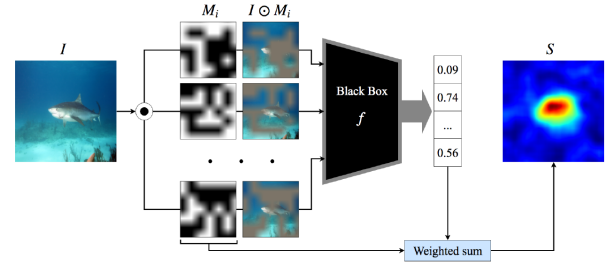


Figure 2. RISE Overview: The input image I is element-wise multiplied with random masks M_i and the masked images are fed to the base model. The saliency map is a linear combination of the masks where the weights are the score of the target class corresponding to the respective masked inputs [41]

3 Evaluation Metrics

As mentioned in the Section. 1, there are different works proposed to assess the XAI methods from different dimensions: faithfulness, localization, false-positives, sensitivity check, and stability. In this section, we review the representative metrics designed for these dimensions and present the detailed mathematical formulations which serve as the guideline for the exact implementations.

3.1 Faithfulness

Saliency methods generates relevance scores w.r.t model predictions assigned to the features (pixels or super-pixels for images). Described in [18], the faithfulness of an explanation refers to whether the relevance scores reflect the true importance. A typical approach for quantifying the property of XAI is through strategical modification on the input according to the explainer indication and monitor the model behaviors. There are several different metrics proposed based on this approach. In this paper, we implement the metric $iAUC$ (termed as *insertion* in the original paper) proposed in [22] and conduct the experiments with it.

• **$iAUC$** Petsiuk *et al.* [22] proposed area under the insertion curve ($iAUC$), which accumulated the probability increase while gradually inserting the features from the original input to a reference input (e.g. a constant-value image or a blurred image). The features from the original input were inserted in the order of high to low relevance score indicated by the explanation method. Given a reference input I_r , the origin input I , and the indexes of features $\{q_0, q_1, q_2, \dots, q_L\}$

that sort the relevance scores from high to low, the calculation of iAUC for a single input can be described as:

$$\begin{aligned} I_{p_0} &= I_r \\ I_{p_{k+1}}[q_k] &= I[q_k], \text{ for } \{k = 0, \dots, L\} \\ \text{iAUC} &= \frac{1}{L+1} \sum_{i=1}^{L+1} (f_c(I_{p_i}) - f_c(I_r)) \end{aligned} \quad (9)$$

where $f_c(\cdot)$ is the model output on class c . Faithful explanations are expected to obtain violent increase at the beginning, and thus the greater AUC.

Faithfulness metrics have the advantages that no extra annotations are needed and the idea of using model behavior changes as a signal of quantifying the explanations is intuitive enough. However, they have a critical issue in the actual calculation: the problem of data shifts. The modifications to the inputs can drag the data out of the learned distribution of the black-box model. Consequently, an enormous change could happen even if low-relevance pixels are removed. This causes unreasonable results when computing the faithfulness of saliency maps, thus further efforts are needed to tackle this issue.

3.2 Localization

For XAI methods that generate relevance scores for features, one of the criteria for the explanations to be good is that it correctly recognize the discriminative features for the model. However, it is hard to find the "ground-truth" discriminative features of a black-box model. In object recognition tasks, a natural assumption is that a well-trained black-box model would make predictions based on the features from the object itself. With this assumption, the evaluation relaxes to whether the explainer correctly localizes the object to be recognized.

• **PG** Zhang *et al.* [41] proposed PG to evaluate the spatial localization capability w.r.t different labels. Taking the images from COCO [15] and PASCAL VOC 2007 [6], the evaluation is simply based on the maximum pixel from the saliency map. If the pixel with the highest score locates inside the ground truth area, it counts as a hit otherwise a miss. Iterating all the images, one can get the number of hits and misses, PG can be simply computed through:

$$\text{PG} = \frac{\#Hits}{\#Hits + \#Misses}. \quad (10)$$

It should be emphasized that the localization of a saliency map refers to the locating capability of a saliency map. Since saliency methods are originally designed to find the features most relevant to model predictions, the saliency map might highlight a few discriminative super-pixels which are considered critical for the decision rather than the whole object. Therefore, a good saliency map is not required to cover the entire object.

3.3 False-positives

As a critical difficulty for evaluating the saliency map is that no ground truth saliency map is available for comparison, an interesting line of works proposed to construct controllable datasets and produce pseudo-ground truth for evaluations [10, 38]. Specifically, Yang and Kim [38] constructed Benchmarking Attribution Methods (BAM) dataset by combining objects from Microsoft COCO [15] and scene images from Miniplaces [43], and proposed three metrics to evaluate the false-positives of XAI methods: Model Contrast Score (MCS), Input dependence Rate (IDR) and Input Independence Rate (IIR). Since IIR can be considered as an extension of stability metric which we shall discuss in the next subsection, we only discuss MCS and IDR here. Taking the definition from [38], the average contribution of a specific concept co on a single image is calculated as:

$$S_{co}(f, I_0) = \frac{1}{\sum M_{co}} \sum E(f, I_0) \odot M_{co} \quad (11)$$

where $M_{co} \in \{0, 1\}^{h \times w}$ represents the binary mask where pixels of concept co take value 1, and 0 otherwise. The black-box model and input image are denoted as f and I_0 . The contribution S_{co} takes average on the Hadamard product of saliency map and binary mask.

Global concept contribution $G_{co}(\cdot)$ is further defined as averaged S_{co} over all the correctly predicted images \mathbb{I}_{corr} :

$$G_{co}(f, \mathbb{I}) = \frac{1}{|\mathbb{I}_{corr}|} \sum_{I_0 \in \mathbb{I}_{corr}} S_{co}(f, I_0) \quad (12)$$

• **MCS** Two models are trained on the same dataset of BAM but with two sets of labels L_o and L_s . Object labels L_o are used to train the object classifier f_o , while scene labels L_s are used to train scene classifier f_s . The object commonly appearing in every scene image is considered as a common feature (CF). For the object classifier f_o , CFs are important features and thus should be assigned higher scores. On the contrary, scene classifier f_s is expected to rely on scenic features rather than the CFs. Since CFs are more important to object classifier f_o than scene classifier f_s , global contribution of CF, $G_{cf}(f_o, \mathbb{I})$ are expected larger than $G_{cf}(f_s, \mathbb{I})$. MCS is defined as the difference between $G_{cf}(f_o, \mathbb{I})$ and $G_{cf}(f_s, \mathbb{I})$.

$$\text{MCS} = G_{cf}(f_o, \mathbb{I}^{cf}) - G_{cf}(f_s, \mathbb{I}^{cf}) \quad (13)$$

MCS measures how differently the CFs are attributed to different classifiers. Object classifiers are supposed to make decisions based on CF, and hence, better explanation should obtain higher MCS.

• **IDR** Considering the scene classifier f_s , if there are two images with the same scenery but with and without CF, the region covered by CF in the image ought to have a smaller contribution to the model prediction than the same area in its counterpart image without CF. IDR calculates the proportion

of saliency maps that assign high scores to CF as follows:

$$\text{IDR} = \frac{1}{|\mathbb{I}^{cf}|} \sum_0^k \mathbb{1}((S_{cf}, I_k^{cf}) > (S_{cf}, I_k^{-cf})) \quad (14)$$

where $I_k^{cf} \in \mathbb{I}^{cf}$ and $I_k^{-cf} \in \mathbb{I}^{-cf}$ are the images with and without the CF. For two images with same scenery, average contribution of pixels covered by CF in the image with CF is compared to the contribution of the same region of its counterpart image without CF. If the former is greater the latter, it counts as a hit. IDR is obtained as the hit rate over the entire dataset, indicating the proportion of images where CFs are assigned high importance scores. Better explanation methods should have smaller IDR.

The constructed datasets provide controllable pseudo-ground-truths for explanations and thus can serve as benchmark datasets for quantifying the faithfulness of explanation methods. However, the generalization of such dataset is questionable: the behaviors of explanation methods on different data and different black-box models can be different, thus the conclusion of the evaluations of explanation methods on the synthetic datasets may not be able to directly generalize to other datasets.

3.4 Sensitivity Check

Besides the attempts to directly design metrics to quantify specific properties of explanation methods, there are works focusing on checking whether the explanation methods have desired sensitivities.

• **Class Sensitivity** is one of the desired sensitivities. If an explanation method is faithful, it should be giving different explanations for different decisions. Take image classification as an example, most of the XAI methods provide saliency maps that highlight the discriminative part as explanations. Different classes usually have different discriminative regions, thus a good explanation method should have clear class sensitivity. Guillaumin *et al.* [7] took classes with the highest and the lowest confidence and computed the similarity between their saliency maps as a metric for class sensitivity (without confusion, we denote the metric as CS in the following text). Given an input I , a classifier f and an explanation method E , CS metric can be then defined as:

$$\begin{aligned} c_{max}, c_{min} &= \arg \max f(I), \arg \min f(I) \\ \text{CS} &= \text{sim}(E(I, f)_{c_{max}}, E(I, f)_{c_{min}}) \end{aligned} \quad (15)$$

where $\text{sim}(\cdot, \cdot)$ is a similarity measurement function, e.g. Pearson correlation.

For a good explanation method, the saliency maps between the classes with the highest score and the lowest score should be very different since these two classes usually do not have similar discrimination strategies. Thus a good explanation method should have CS close to zero or below zero.

We note here, these checks can only be applied as a necessity check, e.g. for a good explanation method, CS must be low, but it does not necessarily work the other way around.

3.5 Stability

In Section. 3.4, we review the works that check whether the XAI methods have the desired sensitivities. Starting from a contrary aspect, some alternative works attempt to evaluate the stability (insensitivity) of XAI methods towards insignificant variations. A good explanation is expected to be stable when an input is perturbed slightly but still has a similar model prediction and confidence distribution. If perceptibly identical images with similar model outputs have completely different saliency maps, it could cause problems in applications. For example, in autonomous driving scenario, passengers may receive completely different explanations, even if there is no obvious change within a few seconds. They will get confused and lose trust in the car system.

• **Max-sensitivity** Yeh *et al.* put forward a simple quantity termed max-sensitivity to measure the stability of an explanation method through the following definition [39]:

$$\text{SENS}_{\max}(E, f, I, r) = \max_{\|\delta\| < r} \| E(f, I + \delta) - E(f, I) \| \quad (16)$$

where r is a predefined parameter indicating the range of perturbation. The attraction of this quantity is that it can be robustly estimated via Monte-Carlo sampling. Another advantage of this quantity is its simplicity in the sense of implementation. In the experiments, we applied this metric definition to quantify the stability of the selected saliency methods.

4 Experiments

To give an overall comparison of the popular methods mentioned in Section. 2, for each dimension discussed in Section. 3, we choose one or two metrics to conduct a set of comparative experiments. All of the experiments are performed across the validation/test set of the two benchmark datasets: Microsoft COCO 2017 [15] and PASCAL VOC 2012 [6], except for false-positives, which we generated an extended BAM (eBAM) dataset to evaluate. For each dataset, two types of pretrained models are explained: ResNet50 [8] and VGG16 [32]. For all the metrics, the overall results are obtained as the average through all the samples in dataset.

4.1 Faithfulness Results

Following the definition of iAUC and the setting described in [22], we conduct the faithfulness experiments with the blurred images set as the perturbed reference images. As argued in [22], compared to setting the reference images as constant-value images, the blurred images could ease the issue of sharp shapes introduction during the insertion. The overall results are shown in Figure. 3.

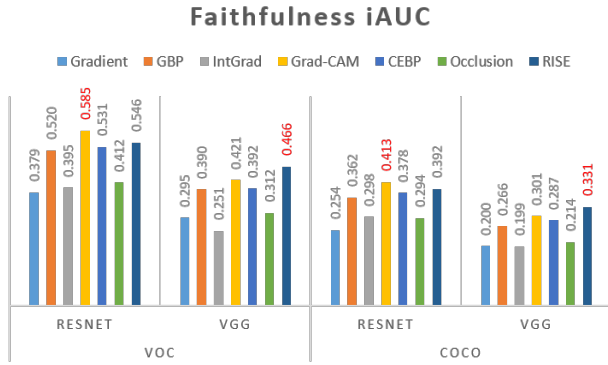


Figure 3. Faithfulness results with iAUC metric across VOC and COCO datasets, with the best methods highlighted. Different saliency methods are represented by different colors. The number above every bar is the overall iAUC.

From Figure. 3, one can see that: (1) RISE and Grad-CAM perform the best in datasets VOC and COCO. Specifically, RISE performs the best for VGG16 in both datasets and Grad-CAM gets the best results for ResNet50. The reason might be that ResNet50 has deeper structure than VGG16 and thus the feature maps from the last convolutional layer of ResNet50 might be more semantic and class discriminative; (2) The ranking of faithfulness for the selected methods is: Grad-CAM \approx RISE > CEBP > GBP > Occlusion > IntGrad \approx Gradient.

To inspect the results, we visualize a few examples in Figure. 4 of the generated saliency maps. The visualization shows that: Grad-CAM indeed captures the objects to be recognized. RISE has similar salient regions as Grad-CAM, but it has diffusive noise in the background. The salient region of CEBP can be seen as a subregion of that of Grad-CAM. Gradient, IntGrad and Occlusion have noisy saliency maps while GBP highlights the edges of the objects clearly.

The reason that Grad-CAM performs better might be that it calculates the attribution of the last convolutional layer, which better capture high-level semantic information. And the reason that RISE performs better than Occlusion might be that the perturbation on RISE are more flexible than Occlusion (does not require to be patch-based perturbation), thus the sampling reservoir can be larger and the sampling results are less noisy and more faithful. IntGrad and Gradient perform the worst because they include negative gradients and the saliency maps are noisier.

Although we chose iAUC as the metric for our faithfulness experiments, the out of distribution issue is still a severe problem. As shown in Figure. 5, the output probability of the third to last subfigure is closed to zero while the last subfigure contains a few more pixels and the output probability is nearly one.

4.2 Localization Results

Referring to [41], we apply PG to quantify the localization of the XAI methods on the object to classify. The overall results are shown in Figure. 6.

From Figure. 6, there are a few conclusions that can be drawn: (1) Grad-CAM and RISE get the best results. The reason behind is likely to be the same as the one analyzed in faithfulness: ResNet50 has deeper network structure; (2) CEBP performs comparably well in ResNet50 as Grad-CAM and RISE. This might be due to the fact that CEBP also propagate the excitation to intermediate convolutional layer rather than the input layer. However for VGG16, CEBP has a significant underperformance compared to Grad-CAM. This might be related to the fact that VGG16 has three fully connected layers and thus be too many nodes to propagate the probability; (3) The rest of the methods have marginally worse performance. As argued in Section. 4.1, Gradient, IntGrad, and Occlusion have noisier saliency maps. As for GBP, although the saliency map is cleaner, it highlights the edges of all objects and therefore may lose localization capability.

From the definition of PG, one can see that it measures whether an explanation indicates the ground truth bounding box. However, as it focuses only on the single point with the highest importance, it cannot well describe situations that the saliency map captures unnecessary information (saliency map of RISE in Figure. 4). To resolve this issue, we revise slightly on the PG by taking this into account. Mathematically, we define a modified metric, that is, the ratio of Intersection between the salient area and the ground truth mask over the Salient Region (IoSR):

$$\text{IoSR} = \frac{M_{GT} \cap SA(E(I, f))}{SA(E(I, f))} \quad (17)$$

where M_{GT} is the ground truth mask and $SA(\cdot)$ is the salient area of a saliency map. In our experiment, $SA(E(I, f))$ is calculated as the $\sum(E(I, f) > \theta \max E(I, f))$, in which θ is a user-defined threshold (default: 0.5).

Iterating through the whole set of data, the result for IoSR is shown as in Figure. 7. Comparing Figure. 6 and Figure. 7, Grad-CAM and CEBP perform comparably well in both implementations. On the contrary, RISE has the smallest score in IoSR while it gets a relatively high score in PG. The reason may lie behind the mechanisms of RISE: masking on the original images could drag the images out of data manifold, thus the resulting probability is not a mere reflection on the information the masks contain but also effects of out-of-distribution. Occlusion is also plagued by this problem and thus Occlusion also has more significant drops on the results than the backpropagation methods.

Although IoSR captures more information than PG, it suffers from the same issues as PG: (1) This metric is unable to distinguish the failure modes of explainer from failure modes of the pretrained model. If the result is good, it does reflect that the pretrained model can recognize the object

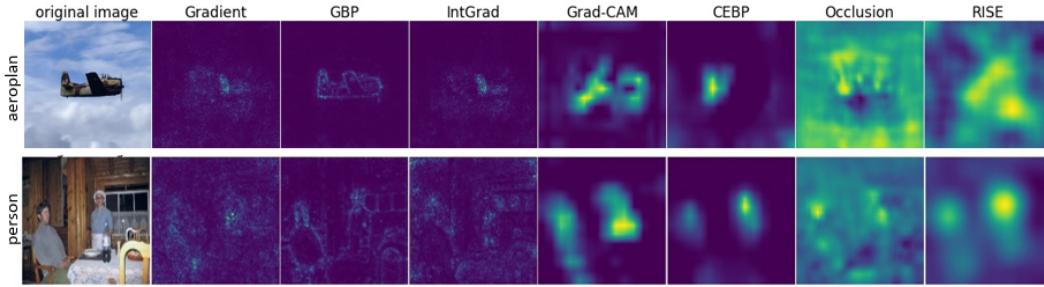


Figure 4. Typical saliency maps of the listed methods. Data samples are from PASCAL VOC and the pretrained model is VGG16.

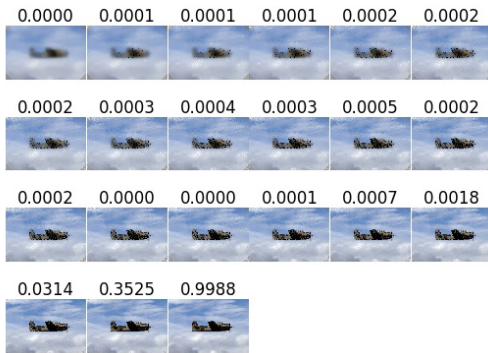


Figure 5. An example that shows the intermediate process of iAUC. The number above each subfigure is the corresponding output probability of the node of interest ("aeroplane" in this example). From upper left to lower right, more and more pixels are inserted in the order of indicated importance of saliency maps.

Localization PG

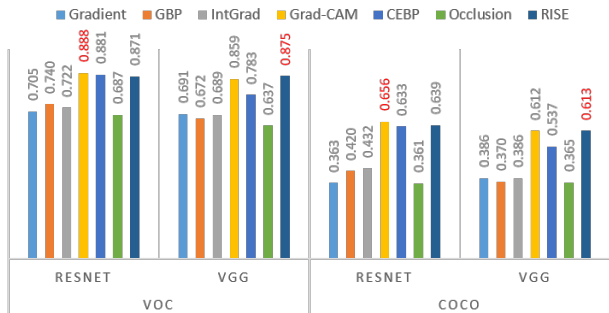


Figure 6. Localization overall results with PG across VOC and COCO datasets with two pretrained models. The best performed saliency methods are highlighted. The number above every bar is the localization result based on PG.

and the explainer can locate the discriminative part of the object. However, if the result is poor, the reason could be either the pretrained model does not understand the object or the explainer fails to find the discriminative region of the

model; (2) The computation requires the human-annotated bounding boxes or segmentation masks. In most cases, this may not be available in classification scenario.

Localization IoSR

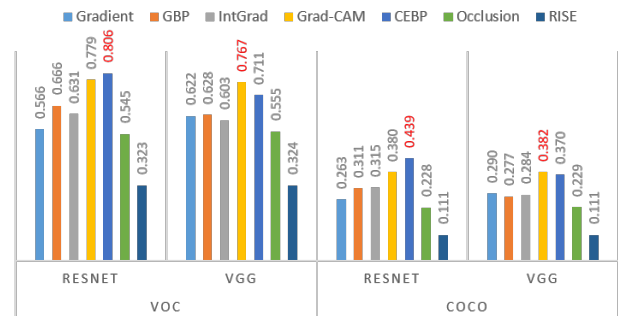


Figure 7. Overall results for localization (IoSR).

4.3 False-Positives Results

In [38], the quality of the explanations were assessed via investigating false high-score attributions on irrelevant features on BAM dataset. However, BAM dataset used in [38] only includes 10 object labels and 10 scene labels, which could lead to weak generalization for benchmarking. In this experiment, we extend BAM to eBAM by leveraging full set of objects from COCO and scenes from Miniplaces, containing 80 objects and 100 scenes.

Following the construction of BAM, objects are extracted, rescaled to between 1/3 and 1/2 of the scene image (128 * 128 in Miniplaces), and randomly placed in the image. After extracting the objects from COCO training and validation set, a huge amount of objects are found unreasonable and defective, i.e., only tiny patches of the object are extracted, without recognizable semantic information. To relieve the impact of such defects, extracted objects are integrated into the black background and fed into Faster-RCNN (pretrained on COCO) [25] for object detection. Only the objects detected with the correct label and confidence higher than 50% are

retained for data synthesis. Numerous data are filtered after detection, we abandon classes containing fewer than 500 samples, remaining 53 object labels. Scenery images could also contain objects. To resolve this problem, scenery images are also inferred through the object detection model. If any object is detected with high confidence (higher than 50%), the image will be discarded. Part of the images are filtered but still remain all the 100 labels. Consequently, the training set is made of 53 object labels and 100 scene labels, resulting in 5300 combined labels and each label contains nearly 500 images, a total of 2,646,328 images as the training set. We inherit the same object and scene labels on the validation set and filter the objects and scenes through the same process, leaving 378,830 images for evaluations. We train ResNet50 [8] and VGG16 [32] on the training set and evaluate MCS as well as IDR of the explaining methods on the validation set. Since perturbation-based methods take a long time on running through such a large validation set, only backpropagation methods are evaluated in this subsection.

Table 1. FP results of backpropagation methods on eBAM

	Model	Gradient	GBP	IntGrad	Grad-CAM	CEBP
$G_{cf}(f_s, \mathbb{I})$	Resnet50	0.019	0.027	0.029	0.261	0.025
	VGG16	0.018	0.009	0.031	0.114	0.030
$G_{cf}(f_o, \mathbb{I})$	Resnet50	0.090	0.050	0.076	0.754	0.293
	VGG16	0.105	0.060	0.079	0.436	0.261
MCS	Resnet50	0.071	0.024	0.046	0.492	0.268
	VGG16	0.088	0.051	0.048	0.320	0.231
MCR	Resnet50	0.310	0.301	0.285	0.205	0.653
	VGG16	0.666	0.630	0.633	0.693	0.774
IDR	Resnet50	0.005	0.201	0.112	0.090	0.203
	VGG16	0.006	0.027	0.124	0.196	0.283

4.3.1 MCS and MCR.

MCS calculates the difference between concept contributions of different classifiers over the dataset. However, relevance scores in saliency maps from different interpreting methods could distribute in different ranges, even after normalization. As seen in Table.1, Grad-CAM tends to assign a higher score than the other explanations, resulting in higher but unfair MCS. To relieve this unfairness, we further introduce Model contrast Ratio (MCR) to compare attribution differences. Given a scene classifier f_s , attributions on CF ought to take a low proportion of the overall saliency map. On the other hand, attributions from an object classifier f_o are expected to focus on the CF region. MCR compares the ratios of CF attributions between f_s and f_o , formulated below:

$$MCR = \frac{1}{|\mathbb{I}_{corr}|} \sum_{I_k \in \mathbb{I}_{corr}} \left(\frac{S_{cf}(f_o, I_k)}{\sum(f_o, I_k)} - \frac{S_{cf}(f_s, I_k)}{\sum(f_s, I_k)} \right) \quad (18)$$

Higher MCR indicates a more accurate explanation. As shown in Table. 1, CEBP outperforms other methods in terms of MCR on both models. Grad-CAM outperforms other methods in terms of MCS, but receive the lowest MCR on Resnet50.

We visualize the saliency maps of f_s and f_o for further checks. Demonstrated in Figure.8, all the backpropagation methods in the experiment exhibit weakly-supervised object localizing capability. Grad-CAM produces low-resolution saliency maps on Resnet50 as the dimension of selected convolutional layer output is $7 \times 7 \times 2048$, while other methods accurately highlight pixels within the CF region. High-score attributions of Grad-CAM result in higher MCS, but in the meanwhile, coarse edges pull down the MCR scores due to misleading attributions outside the objects. Due to higher resolution of selected feature maps in VGG16 ($14 \times 14 \times 512$), Grad-CAM generates more precise saliency maps and results in a competitive MCR score.

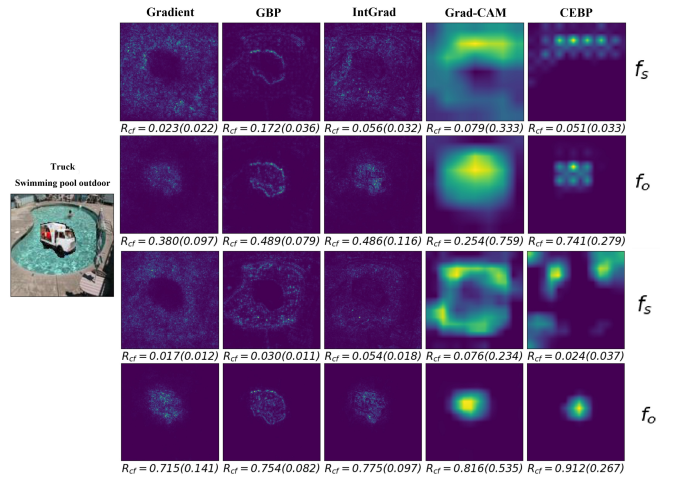


Figure 8. Saliency maps of the same synthetic images explained on object classifier f_o and scene classifier f_s . Objects in the images are expected to be important for f_o but irrelevant for f_s . The title above original images indicates the scene and object. The values below the saliency maps are MCR scores with MCS in parenthesis. The top and the bottom figures demonstrate the results of Resnet50 and VGG16 respectively.

4.3.2 IDR.

Higher IDR indicates that the saliency method assigns higher scores to CF regions which are considered irrelevant in decision making. The baseline of IDR is 50%, representing the performance of randomly attributed saliency maps. As shown in Table. 1, CEBP exhibits unreasonable attributions on both Resnet50 and VGG16 while Gradient performs the best in IDR test (consistent with the conclusion of [38]). Grad-CAM gets the opposite ranking on Resnet50 and VGG16. Figure. 9 demonstrates the saliency maps of images with and without CF. In the example of "airplane-iceberg", Gradient and IntGrad have clear dark spots on the CF, exhibiting better discriminating ability. We notice that GBP assigns a high relevance score to the edge of CF object, as suggested in [2].

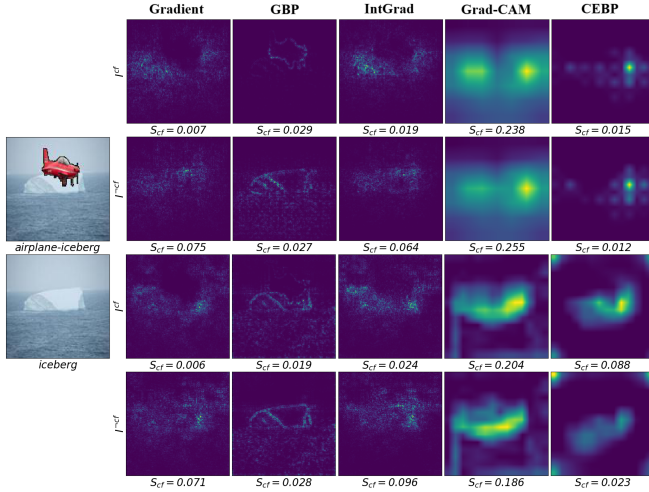


Figure 9. Saliency maps with and without CF. "Airplane" is the CF in scene classification, which should be assigned lower salient scores. The top and the bottom figures demonstrate the results of Resnet50 and VGG16 respectively.

We measure false-positives of explanations on eBAM dataset in this section. To relieve the unfairness introduced by MCS, we propose MCR to compare attributions from different classifiers. Drawing the same conclusion as [38], Gradient performs well in both MCR and IDR measurements, although it only processes a simple backpropagation to produce saliency maps. A different finding is that Grad-CAM falls back on IDR in the experiment on Resnet50, while it is reported as good as Gradient on BAM dataset. This situation indicates that different datasets could lead to different FP results. We also observe different rankings on the same model structure and metrics but with various hyper-parameters. Therefore, generalizing the explanation ranking from eBAM or BAM to other datasets could be questionable. On the other hand, such benchmark could still be considered as a rigorous test to develop new explaining methods.

4.4 Sensitivity Check Results

For the simplicity of the experiments, we choose to measure the class sensitivity of the XAI methods. Following the definition of class sensitivity described in 3.4, we measure the similarity between max-confidence and min-confidence saliency maps. In this work, we apply Pearson correlation to perform experiments for CS. Specifically, smaller correlation, i.e., larger discrepancy, between maximal and minimal confidence saliency map of the original image indicates higher class sensitivity of the explaining method. Figure 10 shows the comparison among CS of the selected saliency methods applied across two datasets and two pretrained models.

From the overall experimental results in Figure 10, we can see that: Grad-CAM, RISE, and Occlusion perform fairly well w.r.t class sensitivity as the CS scores are nearly zero or below

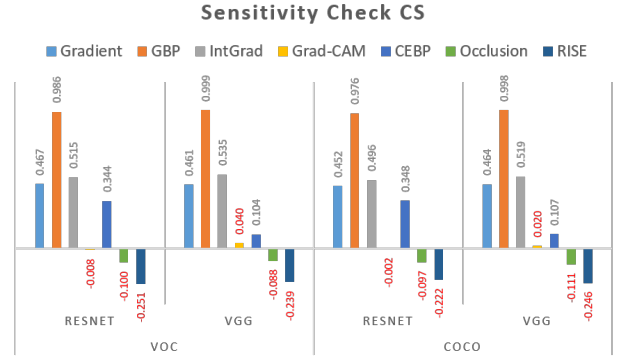


Figure 10. Sensitivity check results with CS (calculated by Pearson correlation) across two datasets and two pretrained models. Well-performed saliency methods that have negative are highlighted.

zero. GBP has the worst class sensitivity. For the rest of the methods, the ranking is CEBP > Gradient > IntGrad. Figure 11 demonstrates an example from COCO dataset and the visual comparison supports the ranking above. The saliency maps of max-confidence label "cat" and min-confidence label "bed" are almost identical from GBP. As explained by [2], GBP acts like an edge detector, and thus results in poor class sensitivity. Another interesting result suggested in Figure 10 is that perturbation-based methods have negative class sensitivity. As shown in Figure 11, the saliency maps of max-confidence and min-confidence labels highlight complementary regions.

4.5 Stability Results

Following the definition of $SENS_{max}$ reviewed in Section 3.5, we quantitatively measure the stability for the saliency methods mentioned in Section 2. One might notice that $SENS_{max}$ depends on the radius of perturbation. To investigate such dependence, we first varied the radius and perturbation and get $SENS_{max}$ on few examples (the results are averages across five examples) and get the results shown in Figure 12.

As demonstrated in Figure 12, metric $SENS_{max}$ strongly depends on the choice of radius of perturbation. This indicates that stability of a saliency method varies w.r.t the strength of perturbation. In the cases of small perturbation radius, RISE and Occlusion get smaller sensitivity thus show higher stability while Gradient exhibits high sensitivity. However, when perturbation becomes stronger, the curves start to cross with each other. In the stronger perturbation region, CEBP and RISE exhibit the best stability. In real life applications, the stability of saliency methods should be measured within the range of the practical perturbation.

Considering a small perturbation region (as the definition of stability is on the insignificant perturbation), the

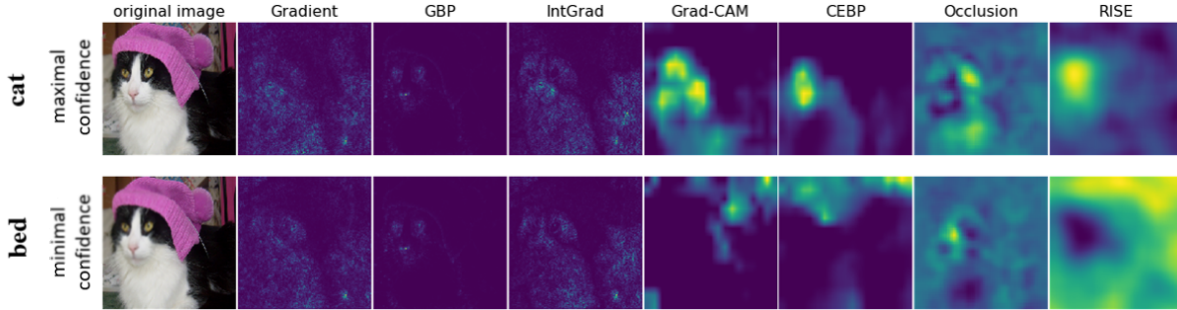


Figure 11. Typical maximal (1st row) and minimal (2nd row) confidence saliency maps of the listed methods. Data samples are from COCO and the pretrained model is VGG16.

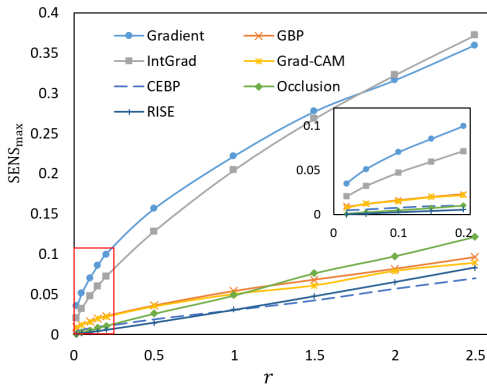


Figure 12. $SENS_{max}$ vs. perturbation radius r relation. The x -axis is the settings of perturbation radius during experiments and the y -axis is the calculated results for $SENS_{max}$. The inset is the zoom-in view of the rectangular framed region. Different curves represent different saliency methods behavior. The results are obtained from averaging five examples from PASCAL VOC and the pretrained model is VGG16.

$SENS_{max}$ results across different datasets and different pre-trained models are obtained in Figure. 13. Figure 13 shows that Gradient and IntGrad have the marginally worse stability compared to others. The possible reason for this is that these two methods contains negative gradients and the perturbation noise most likely has negative contribution to the final output. Other methods would not suffer from this issue. RISE and Grad-CAM exhibit the strongest stability in Resnet50 while RISE and Occlusion behave the best for VGG16. The stability of Grad-CAM may also be related to the fact that it calculates the attribution of last convolutional layer. As for RISE and Occlusion, the calculation process already involve perturbation and thus a slight perturbation on the input may not have significant effects. Another finding from Figure. 13 is that this quantity does not show significant variations w.r.t to datasets: not only the relative rankings are

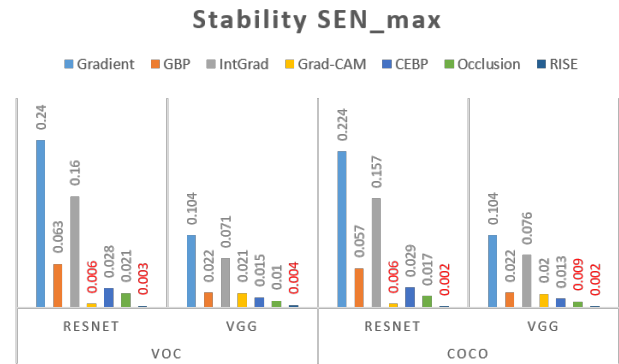


Figure 13. Stability results from $SENS_{max}$ in small perturbation region with perturbation radius $r = 0.2$ across two different datasets and two pretrained models. The results are averaged across 50 randomly selected examples from both datasets.

the same for both datasets, the values for different methods are also nearly identical across the two datasets.

4.6 Summary of Experimental Results

In this subsection, we summarize the above experimental results. To better show these results, we average the four experimental results across the two datasets and two pre-trained models of faithfulness, localization, sensitivity check, and stability. We then get the results in Table. 2, with the marginally better methods highlighted for every metric. In terms of faithfulness, Grad-CAM and RISE perform the best. As for sensitivity check, Grad-CAM, RISE, and Occlusion have excellent performance while GBP has almost no class sensitivity. And RISE has the best stability while Gradient seems to be sensitive to insignificant perturbation. From Table. 1, Gradient exhibits solid performance in the false-positives experiment. Advanced methods derived from Gradient obtain lower IDR. According to the results above, we find no saliency method could serve as a silver bullet in

saliency-based problems, explaining methods need carefully selected depending on the desired properties.

Table 2. Averaged Experimental Results Across Two Datasets and Two Pretrained Models

XAI methods	Localization (PG)	Localization (IoSR)	Faithfulness (iAUC)	Sensitivity Check (CS)	Stability
Gradient	0.536	0.435	0.282	0.461	0.168
GBP	0.551	0.47	0.384	0.99	0.041
IntGrad	0.557	0.458	0.286	0.516	0.116
Grad-CAM	0.754	0.577	0.43	0.013	0.013
CEBP	0.709	0.582	0.397	0.226	0.021
Occlusion	0.512	0.389	0.308	-0.099	0.014
RISE	0.75	0.217	0.434	-0.239	0.002

5 Utilization of XAI Methods and Metrics

In the previous section, we mainly discuss the overall performance of the XAI methods with the metrics reviewed in Section 3. In this section, we present a case study of the XAI methods as well as its metrics in actual model analysis – *Clever Hans Detection*. "Clever Hans" originally refers to a horse that was believed to be able to perform arithmetic calculations. Later it was discovered that instead of conducting actual calculation, this horse was giving the correct answers based on the unintended gestures of its trainer. Similar Clever Hans phenomena also occur in machine learning, that the trained machine make decisions based on spurious correlations, e.g., the trained Fisher Vector classifier classifies an image to be "horse" based on the watermark [13]. A model that learned "Clever Hans"-type decision strategy will likely fail to provide correct classification for new datasets without such spurious correlations. Thus it is essential to find out the Clever Hans cases of the model before actual deployment. However, conducting visual inspections one by one on the explanations of whole dataset can be laborious costive and most likely unable to execute. In this section, we propose a simple way to find out the examples that show Clever Hans effects in a classification scenario with XAI methods and measuring metrics.

Revisiting the concept of Clever Hans, such examples would likely show high classification confidence but the classification basis for them are "wrong". A faithful explanation help to locate such classification basis. Thus, borrowing the metrics studied in the above sections, we can have a simple formula to find out the Clever Hans examples $\{I_{CH}\}$ from a large dataset:

$$\{I_{CH}\} = \{I_{f_c > \theta_c}\} \cap \{I_{M_{loc} < \theta_l}\} \cap \{I_{M_{faith} > \theta_f}\} \quad (19)$$

where $\{I_{f_c > \theta_c}\}$ refers to the images set with model output f_c greater than a threshold θ_c , and $\{I_{M_{loc} < \theta_l}\}$ and $\{I_{M_{faith} > \theta_f}\}$ refer to the image set with metric of localization lower than a threshold θ_l and metric of faithfulness greater that a threshold θ_f , respectively. Notably, the metric of faithfulness is applied here to make sure the explanation is faithful enough.



Figure 14. Selected examples from VOC dataset that show Clever Hans phenomenon. The predicted labels for rows from top to bottom are "person", "aeroplane", and "chair", respectively. The predicted outputs and the iAUC metric results are listed below each figure and the PG results for all these examples are 0. The explanation method we apply here is Grad-CAM and the black-box model is ResNet50.

Based on Equation. (19), we find a set of examples that show Clever Hans phenomenon. Figure. 14 shows a few representative examples of them. In these examples, although the black-box model gives correct predictions, the found explainable classification bases are unreasonable. For instance, although the model correctly recognizes "person", its bases are the presence of "horse" or "motorbike" as shown in the first row in Figure. 14. This may be caused by the concurrence of "person" and "horse" or "motorbike" in the training set. Other selected interesting examples from COCO are shown in Figure. 15. The model predicts "tennis racket", "baseball glove", and "skis" based on tennis court, the outfit of the baseball player, and the skis poles, respectively.

As we mentioned that "Clever Hans"-type classification strategies may cause misclassification when dealing with data without spurious correlations. As an investigation of this effect, we check on the failure modes on the test dataset. We list a few examples in Figure. 16, where the black-box model makes false-positive predictions due to the presence of "Clever Hans"-type features. An image containing only "motorbike" is predicted to be positive about the presence of "person" because the model takes the presence of "motorbike" feature as a classification base for "person".



Figure 15. Selected examples from COCO dataset that show Clever Hans phenomenon. The predicted outputs and the iAUC metric results are listed below each figure and the PG results for all these examples are 0. The classification model here is ResNet50 for COCO.



Figure 16. False-positive examples due to "Clever Hans"-type features.

6 Conclusions and Outlook

In conclusion, we first filter a set of metrics that are proposed to quantify the quality of XAI methods from five different perspectives. Then, we conduct a thorough set of experiments to quantitatively evaluate some of the popular saliency methods with these metrics. The experimental results show that no single method can achieve the best results from all perspectives. In application, users need to choose an explanation method according to their priorities. Nevertheless, Grad-CAM and RISE perform quite well for all metrics except false-positives for Grad-CAM and IoSR of localization for RISE. This is due to their intrinsic natures: the resolution of Grad-CAM is very low compared to other backpropagation

methods, and as a perturbation method RISE usually has dispersive saliency maps.

Along with the experiments, we propose a new metric – Intersection between the salient region and the bounding box over Salient Region (IoSR) for localization to capture whether the saliency map is compact. And to calculate the false-positives, we expand the original BAM dataset to accommodate more objects and more scenes. Last but not least, we propose a simple application of a combination of metrics to locate Clever Hans examples and analyze the failure modes of the black-box models.

Our last comment is that, although the community may expect a universal metric set to evaluate all explanation methods, nature and applying scenario of XAI might turn us down. The ultimate purpose of XAI, arguably, is to provide necessary information to satisfy the causal curiosity of the user to build trust. To this end, fair evaluation can only be effectively conducted under a fixed scenario and mode setting. Moreover, since the explanation is for human users to build their understanding and trust on the machine side, a sound evaluation metric should reside deeply on cognitive rationales, and currently, there is an observable gap between the cognitive findings and their computational implementations. We believe continuous research attention in this direction will finally bring about insightful results. As for the applications of XAI, we also note here finding Clever Hans examples in the datasets as shown in Section. 5 can not only help diagnose the black-box models, but might also be applied to further improve the generalization and the performance of the model through simple data modification, e.g. masking the salient part of the examples that show Clever Hans phenomena, and retrain the black-box model.

References

- [1] Amina Adadi and Mohammed Berrada. 2018. Peeking inside the black-box: A survey on Explainable Artificial Intelligence (XAI). *IEEE Access* 6 (2018), 52138–52160.
- [2] Julius Adebayo, Justin Gilmer, Michael Muelly, Ian Goodfellow, Moritz Hardt, and Been Kim. 2018. Sanity checks for saliency maps. In *Advances in Neural Information Processing Systems*. 9505–9515.
- [3] Naama Boer, Daniel Deutch, Nave Frost, and Tova Milo. 2020. Personal insights for altering decisions of tree-based ensembles over time. *Proceedings of the VLDB Endowment* 13, 6 (2020), 798–811.
- [4] Ann-Kathrin Dombrowski, Maximillian Alber, Christopher Anders, Marcel Ackermann, Klaus-Robert Müller, and Pan Kessel. 2019. Explanations can be manipulated and geometry is to blame. In *Advances in Neural Information Processing Systems*. 13567–13578.
- [5] Finale Doshi-Velez and Been Kim. 2017. Towards a rigorous science of interpretable machine learning. *arXiv preprint arXiv:1702.08608* (2017).
- [6] M. Everingham, L. Van Gool, C. K. I. Williams, J. Winn, and A. Zisserman. [n. d.]. The PASCAL Visual Object Classes Challenge 2007 (VOC2007) Results. <http://www.pascal-network.org/challenges/VOC/voc2007/workshop/index.html>.
- [7] Matthieu Guillaumin and Vittorio Ferrari. 2012. Large-scale knowledge transfer for object localization in imagenet. In *2012 IEEE Conference on Computer Vision and Pattern Recognition*. IEEE, 3202–3209.

- [8] Kaiming He, Xiangyu Zhang, Shaoqing Ren, and Jian Sun. 2016. Deep residual learning for image recognition. In *Proceedings of the IEEE conference on computer vision and pattern recognition*. 770–778.
- [9] Robert R. Hoffman, Shane T. Mueller, Gary Klein, and Jordan Litman. 2018. Metrics for explainable AI: Challenges and prospects. *arXiv preprint arXiv:1812.04608* (2018).
- [10] Been Kim, Martin Wattenberg, Justin Gilmer, Carrie Cai, James Wexler, Fernanda Viegas, and Rory Sayres. 2017. Interpretability beyond feature attribution: Quantitative testing with concept activation vectors (tcav). *arXiv preprint arXiv:1711.11279* (2017).
- [11] Sanjay Krishnan and Eugene Wu. 2017. Palm: Machine learning explanations for iterative debugging. In *Proceedings of the 2nd Workshop on Human-In-the-Loop Data Analytics*. 1–6.
- [12] Alex Krizhevsky, Ilya Sutskever, and Geoffrey E. Hinton. 2012. ImageNet classification with deep convolutional neural networks. In *Advances in Neural Information Processing Systems*. 1097–1105.
- [13] Sebastian Lapuschkin, Stephan Wäldchen, Alexander Binder, Grégoire Montavon, Wojciech Samek, and Klaus-Robert Müller. 2019. Unmasking clever hans predictors and assessing what machines really learn. *Nature communications* 10, 1 (2019), 1–8.
- [14] Xiao-Hui Li, Caleb Chen Cao, Yuhan Shi, Wei Bai, Han Gao, Luyu Qiu, Cong Wang, Yuanyuan Gao, Shenjia Zhang, Xun Xue, and Lei Chen. 2020. A Survey of Data-driven and Knowledge-aware eXplainable AI. *IEEE Transactions on Knowledge and Data Engineering* (2020).
- [15] Tsung-Yi Lin, Michael Maire, Serge Belongie, James Hays, Pietro Perona, Deva Ramanan, Piotr Dollár, and C Lawrence Zitnick. 2014. Microsoft coco: Common objects in context. In *European conference on computer vision*. Springer, 740–755.
- [16] Scott M. Lundberg and Su-In Lee. 2017. A Unified Approach to Interpreting Model Predictions. In *Advances in Neural Information Processing Systems* 30. Curran Associates, Inc., 4765–4774.
- [17] Shiqing Ma, Yingqi Liu, Wen-Chuan Lee, Xiangyu Zhang, and Ananth Grama. 2018. MODE: automated neural network model debugging via state differential analysis and input selection. In *Proceedings of the 2018 26th ACM Joint Meeting on European Software Engineering Conference and Symposium on the Foundations of Software Engineering*. 175–186.
- [18] David Alvarez Melis and Tommi Jaakkola. 2018. Towards robust interpretability with self-explaining neural networks. In *Advances in Neural Information Processing Systems*. 7775–7784.
- [19] Anh Nguyen, Alexey Dosovitskiy, Jason Yosinski, Thomas Brox, and Jeff Clune. 2016. Synthesizing the preferred inputs for neurons in neural networks via deep generator networks. In *Advances in neural information processing systems*. 3387–3395.
- [20] Allen Ordookhanians, Xin Li, Supun Nakandala, and Arun Kumar. 2019. Demonstration of Krypton: optimized CNN inference for occlusion-based deep CNN explanations. *Proceedings of the VLDB Endowment* 12, 12 (2019), 1894–1897.
- [21] Aditya Parameswaran. 2019. Enabling data science for the majority. *Proceedings of the VLDB Endowment* 12, 12 (2019), 2309–2322.
- [22] Vitali Petsiuk, Abir Das, and Kate Saenko. 2018. Rise: Randomized input sampling for explanation of black-box models. *arXiv preprint arXiv:1806.07421* (2018).
- [23] Kun Qian, Lucian Popa, and Prithviraj Sen. 2019. SystemER: a human-in-the-loop system for explainable entity resolution. *Proceedings of the VLDB Endowment* 12, 12 (2019), 1794–1797.
- [24] Sylvestre-Alvise Rebuffi, Ruth Fong, Xu Ji, and Andrea Vedaldi. 2020. There and Back Again: Revisiting Backpropagation Saliency Methods. In *Proceedings of the IEEE/CVF Conference on Computer Vision and Pattern Recognition*. 8839–8848.
- [25] Shaoqing Ren, Kaiming He, Ross Girshick, and Jian Sun. 2015. Faster r-cnn: Towards real-time object detection with region proposal networks. In *Advances in neural information processing systems*. 91–99.
- [26] Marco Tulio Ribeiro, Sameer Singh, and Carlos Guestrin. 2016. Why should i trust you?: Explaining the predictions of any classifier. In *Proceedings of the 22nd ACM SIGKDD international conference on knowledge discovery and data mining*. ACM, 1135–1144.
- [27] Olga Russakovsky, Jia Deng, Hao Su, Jonathan Krause, Sanjeev Satheesh, Sean Ma, Zhiheng Huang, Andrej Karpathy, Aditya Khosla, Michael Bernstein, Alexander C. Berg, and Li Fei-Fei. 2015. ImageNet Large Scale Visual Recognition Challenge. *International Journal of Computer Vision (IJCV)* 115, 3 (2015), 211–252. <https://doi.org/10.1007/s11263-015-0816-y>
- [28] Wojciech Samek, Alexander Binder, Grégoire Montavon, Sebastian Lapuschkin, and Klaus-Robert Müller. 2016. Evaluating the visualization of what a deep neural network has learned. *IEEE transactions on neural networks and learning systems* 28, 11 (2016), 2660–2673.
- [29] Thibault Sellam, Kevin Lin, Ian Huang, Michelle Yang, Carl Vondrick, and Eugene Wu. 2019. Deepbase: Deep inspection of neural networks. In *Proceedings of the 2019 International Conference on Management of Data*. 1117–1134.
- [30] Ramprasaath R. Selvaraju, Michael Cogswell, Abhishek Das, Ramakrishna Vedantam, Devi Parikh, and Dhruv Batra. 2017. Grad-CAM: Visual explanations of deep networks via gradient-based localization. In *Proceedings of the IEEE International Conference on Computer Vision*. 618–626.
- [31] Karen Simonyan, Andrea Vedaldi, and Andrew Zisserman. 2013. Deep inside convolutional networks: Visualising image classification models and saliency maps. *arXiv preprint arXiv:1312.6034* (2013).
- [32] Karen Simonyan and Andrew Zisserman. 2014. Very deep convolutional networks for large-scale image recognition. *arXiv preprint arXiv:1409.1556* (2014).
- [33] Jost Tobias Springenberg, Alexey Dosovitskiy, Thomas Brox, and Martin Riedmiller. 2014. Striving for simplicity: The all convolutional net. *arXiv preprint arXiv:1412.6806* (2014).
- [34] M Sundararajan, A Taly, and Q Yan. [n. d.]. Axiomatic attribution for deep networks. arXiv 2017. *arXiv preprint arXiv:1703.01365* ([n. d.]).
- [35] Manasi Vartak, Joana M F. da Trindade, Samuel Madden, and Matei Zaharia. 2018. Mistique: A system to store and query model intermediates for model diagnosis. In *Proceedings of the 2018 International Conference on Management of Data*. 1285–1300.
- [36] Athanasios Voulodimos, Nikolaos Doulamis, Anastasios Doulamis, and Eftychios Protopapadakis. 2018. Deep learning for computer vision: A brief review. *Computational intelligence and neuroscience* 2018 (2018).
- [37] Fan Yang, Mengnan Du, and Xia Hu. 2019. Evaluating explanation without ground truth in interpretable machine learning. *arXiv preprint arXiv:1907.06831* (2019).
- [38] Mengjiao Yang and Been Kim. 2019. BIM: Towards quantitative evaluation of interpretability methods with ground truth. *arXiv preprint arXiv:1907.09701* (2019).
- [39] Chih-Kuan Yeh, Cheng-Yu Hsieh, Arun Suggala, David I Inouye, and Pradeep K Ravikumar. 2019. On the (in) fidelity and sensitivity of explanations. In *Advances in Neural Information Processing Systems*. 10967–10978.
- [40] Matthew D Zeiler and Rob Fergus. 2014. Visualizing and understanding convolutional networks. In *European conference on computer vision*. Springer, 818–833.
- [41] Jianming Zhang, Sarah Adel Bargal, Zhe Lin, Jonathan Brandt, Xiaohui Shen, and Stan Sclaroff. 2018. Top-down neural attention by excitation backprop. *International Journal of Computer Vision* 126, 10 (2018), 1084–1102.
- [42] Bolei Zhou, Aditya Khosla, Agata Lapedriza, Aude Oliva, and Antonio Torralba. 2016. Learning deep features for discriminative localization. In *Proceedings of the IEEE conference on computer vision and pattern recognition*. 2921–2929.
- [43] Bolei Zhou, Agata Lapedriza, Aditya Khosla, Aude Oliva, and Antonio Torralba. 2017. Places: A 10 million Image Database for Scene Recognition. *IEEE Transactions on Pattern Analysis and Machine Intelligence* (2017).